Advances in
Geo-Energy Research

Vol. 17, No. 2, p. 162-175, 2025

Original article

Enhanced oil recovery via CO_2 flooding in tight reservoirs: A pore-scale analysis

Jinbao Liu[1,2], Danting Xiao[1,2], Jia Li[1,2], Linsong Cheng[1,2], Han Wang[1], Jianchao Cai[1]*

[1] *State Key Laboratory of Petroleum Resources and Engineering, China University of Petroleum, Beijing 102249, P. R. China*
[2] *College of Petroleum Engineering, China University of Petroleum, Beijing 102249, P. R. China*

Keywords:
CO_2 flooding
tight reservoirs
lattice Boltzmann method
molecular diffusion
viscous flow

Cited as:
Liu, J., Xiao, D., Li, J., Cheng, L., Wang, H., Cai, J. Enhanced oil recovery via CO_2 flooding in tight reservoirs: A pore-scale analysis. Advances in Geo-Energy Research, 2025, 17(2): 162-175.
https://doi.org/10.46690/ager.2025.08.07

Abstract:
CO_2 flooding has become a key technology for enhancing oil recovery in tight reservoirs, with great application potential. However, certain microscopic mechanisms of this technology still need to be further clarified. In this work, a multi-component and multi-phase lattice Boltzmann model based on the pseudopotential scheme is constructed considering different CO_2 flooding behaviors and verified for both immiscible and miscible phases, showing good agreement. On this basis, the effects of capillary numbers, extreme wetting at different velocities, Péclet numbers and injection patterns under fractured conditions on the CO_2 flooding process are systematically investigated. The results show that a larger capillary number enhances the displacement effect, whereas an excessively large value tends to cause viscous fingering, leading to accelerated CO_2 breakthrough. High-velocity extreme wetting conditions result in a higher displacement effect than low-velocity conditions. Moreover, an increase in displacement velocity weakens the wetting effect dominated by capillary force, thereby reducing the difference in oil recovery observed under high-velocity extreme wetting conditions. Different Péclet numbers dominate different fluid transport mechanisms. When the Péclet number is around the unity, the synergistic effects of molecular diffusion and viscous flow are balanced, jointly dominating fluid transport. The pore-fracture combined injection mode integrates the advantages of pore and fracture injections and effectively delays CO_2 breakthrough in the fracture system, resulting in an optimal displacement effect. This model can be extended to research on multiphase flow in tight and shale reservoirs as well as CO_2 geological sequestration.

---

1. Introduction

Tight oil reservoirs, characterized by ultra-low permeability, abundant micro-nano pore throats and complex pore structures, pose significant challenges to conventional waterflooding-based enhanced oil recovery (EOR) techniques (Longde et al., 2019; Milad et al., 2021; Liu, 2023). Owing to its superior miscibility, low viscosity and the associated environmental benefits, CO_2 injection has been widely adopted in secondary recovery processes for tight oil reservoirs (Ozowe et al., 2023; Li et al., 2024; Yin and Zhang, 2024) and demonstrated remarkable potential for EOR. Importantly, CO_2 injection contributes to effective greenhouse gas emission reduction, highlighting its dual advantages in unconventional hydrocarbon development and carbon capture, utilization and storage applications (Zhang et al., 2022; Jia et al., 2023; Zhang et al., 2023; Wang et al., 2024). However, compared to the well-defined EOR mechanisms of water flooding, the underlying microscale mechanisms of CO_2-EOR remain unclear.

Current research on CO_2-EOR mechanisms primarily employs experiments, molecular dynamics simulations, and pore-scale numerical modeling. Experimental approaches can reveal the flow behavior and phase-change mechanisms of CO_2 in

---

Yandy Scientific Press

*Corresponding author.
E-mail address: liujinbaods@163.com (J. Liu); xiao_danting@126.com (D. Xiao); lj1126lj@163.com (J. Li); lscheng@cup.edu.cn (L. Cheng); hanwang@cup.edu.cn (H. Wang); caijc@cup.edu.cn (J. Cai).

Received June 23, 2025; revised July 19, 2025; accepted August 5, 2025; available online August 9, 2025.

porous media at the microscale (Habibi et al., 2017; Chen et al., 2022b; Zuo et al., 2023); however, their high cost, long duration and poor reproducibility restrict the widespread application of these approaches (Gogoi and Gogoi, 2019). Molecular dynamics simulations can elucidate the molecular-scale mechanisms, including CO_2 dissolution, diffusion and adsorption, but they demand substantial computational resources and are limited to extremely small spatial scales (Wang et al., 2020; Zhang et al., 2021; Cai et al., 2024). In contrast, pore-scale numerical simulations offer a balanced solution that maintains high physical fidelity while optimizing computational efficiency and scalability (Frank et al., 2018; Zhao et al., 2022; Zhou et al., 2024). The lattice Boltzmann method (LBM), as a representative pore-scale direct numerical simulation technique, solves the evolution equation of fluid particle distribution functions in discrete velocity space, inherently capturing the fluid-fluid and fluid-solid interactions (Yang and Boek, 2013; Diao et al., 2021). This approach demonstrates distinct advantages in handling complex porous structures, arbitrary boundary geometries, multiphase interface evolution, and multi-physics coupling. Moreover, the algorithmic simplicity of this method facilitates efficient parallel implementation on high-performance computing platforms (Bakhshian et al., 2019; Chen et al., 2022a).

The LBM has also been extensively applied to simulate multiphase and multicomponent flows in porous media, where the capillary number and wettability serve as two pivotal control parameters for evaluating immiscible flow dynamics. Regarding the simulation of gas-water displacement in porous media, some studies have classified different displacement stages, such as viscous fingering, capillary fingering, and stable displacement, on basis of the capillary number (Wang et al., 2023a, 2023b). The LBM simulation results for these stages show good agreement with the experimental data, validating the reliability of LBM in modeling microscopic immiscible displacement processes (Ezzatneshan and Goharimehr, 2021). Further research has incorporated wettability into capillary number analysis, employing LBM to simulate the drainage processes in both two-dimensional (2D) and three-dimensional porous media. These studies systematically investigated the regulatory role of the capillary number in determining the saturation of wetting and non-wetting phases, providing new insights into the fluid trapping mechanisms induced by the coupled effects of capillary number and wettability (Michels et al., 2021). Due to the great diversity of mineral types in reservoirs, wettability can also exhibit significant variations (Shi et al., 2023; Wang and Chang, 2024). Building on this fact, some studies further analyzed the impact of heterogeneous wettability on the relative permeability of oil and water, offering novel perspectives on immiscible flow at the nanoscale (Wang et al., 2022). Other studies integrated LBM with the Darcy-Brinkman-Stokes method to examine waterflooding processes in fractured-vuggy reservoirs under mixed-wettability conditions (Liu et al., 2024). While these researches clearly demonstrated the dominant role of wettability and capillary number in governing fluid distribution patterns and preferential flow pathways, there remains a paucity of LBM literature on CO_2 immiscible displacement, particularly regarding the breakthrough of displacing fluids induced by capillary numbers and scenarios of extreme wettability under different velocities. There has been relatively limited LBM-related literature reporting on miscible flows. Some studies have analyzed the influence mechanism of heterogeneous structures containing fractures and pores on the CO_2 huff-n-puff process, quantitatively characterizing the oil and gas migration patterns during CO_2 huff-and-puff (Zhang et al., 2024). On the other hand, in-depth investigations into CO_2-oil fine miscibility were conducted, with CO_2 adsorption incorporated into the process; however, the scalability of this model is relatively limited (Wang et al., 2025). These limited LBM studies on miscible flows are largely confined to periodic flow boundaries and primarily focus on evaluating the effect of molecular diffusion on oil recovery. At the same time, LBM-related literature regarding CO_2 miscible displacement, that incorporates the convection-diffusion mechanism and different fracture-pore injection patterns, remains relatively scarce.

To address the above research gap, this study proposes a multicomponent multiphase pseudopotential LBM model that simulates various CO_2 displacement behaviors under both miscible and immiscible conditions within a unified framework. A systematic analysis is performed to examine the effects of capillary number, extreme wettability at varying velocities, convection-diffusion competition mechanism, and fracture-pore injection patterns on CO_2 displacement processes while elucidating the underlying microscopic mechanisms and governing principles under different influencing factors. The findings provide the theoretical and computational foundations for EOR in tight and shale oil reservoirs.

2. Methodology

As a mesoscopic simulation method based on molecular dynamics theory, the LBM can effectively reveal the complex interaction mechanisms between fluid-fluid and fluid-solid interactions at the pore scale. To investigate two-phase displacement behavior and the associated flow dynamics in heterogeneous porous media, a multicomponent multiphase pseudopotential model with multiple relaxation times (MRT) is constructed. The governing evolution equation for the MRT-LBM can be expressed as follows (Lallemand and Luo, 2000; Chai and Shi, 2020):

$$\begin{aligned} &f_{\sigma,\alpha}(\mathbf{x}+\mathbf{e}_\alpha \Delta t, t+\Delta t) - f_{\sigma,\alpha}(\mathbf{x},t) = \\ &-\mathbf{M}^{-1}\mathbf{\Lambda}\mathbf{M}\left[f_{\sigma,\beta}(\mathbf{x},t) - f^{\mathrm{eq}}_{\sigma,\beta}(\mathbf{x},t)\right] + \Delta t \mathbf{F}_{\sigma,\alpha}(\mathbf{x},t) \end{aligned} \tag{1}$$

where $f_{\sigma,\alpha}(\mathbf{x},t)$ and $f^{\mathrm{eq}}_{\sigma,\alpha}(\mathbf{x},t)$ represent the density distribution function and the equilibrium density distribution function corresponding to the discrete direction α and component σ at the node position $\mathbf{x}$ at time t, respectively; Δt is the time step; and $\mathbf{F}_\sigma$ represents the total external force.

In the D2Q9 model, $\mathbf{e}_\alpha$ denotes velocity at the α direction, expressed as:

$$\mathbf{e}_\alpha = \begin{cases} 0, & \alpha = 0 \\ \left(\cos\dfrac{(\alpha-1)\pi}{2}, \sin\dfrac{(\alpha-1)\pi}{2}\right), & \alpha = 1,2,3,4 \\ \sqrt{2}\left(\cos\left[\dfrac{(\alpha-5)\pi}{2}+\dfrac{\pi}{4}\right], \sin\left[\dfrac{(\alpha-5)\pi}{2}+\dfrac{\pi}{4}\right]\right), & \alpha = 5,6,7,8 \end{cases} \tag{2}$$

Among them, $\mathbf{M}$ and $\boldsymbol{\Lambda}$ represent the transformation matrix and the diagonal relaxation matrix, respectively, given by:

$$\mathbf{M} = \begin{bmatrix} 1 & 1 & 1 & 1 & 1 & 1 & 1 & 1 & 1 \\ -4 & -1 & -1 & -1 & -1 & 2 & 2 & 2 & 2 \\ 4 & -2 & -2 & -2 & -2 & 1 & 1 & 1 & 1 \\ 0 & 1 & 0 & -1 & 0 & 1 & -1 & -1 & 1 \\ 0 & -2 & 0 & 2 & 0 & 1 & -1 & -1 & 1 \\ 0 & 0 & 1 & 0 & -1 & 1 & 1 & -1 & -1 \\ 0 & 0 & -2 & 0 & 2 & 1 & 1 & -1 & -1 \\ 0 & 1 & -1 & 1 & -1 & 0 & 0 & 0 & 0 \\ 0 & 0 & 0 & 0 & 0 & 1 & -1 & 1 & -1 \end{bmatrix} \tag{3}$$

$$\boldsymbol{\Lambda} = \mathrm{diag}\left(\tau_\rho^{-1}, \tau_e^{-1}, \tau_\zeta^{-1}, \tau_j^{-1}, \tau_q^{-1}, \tau_j^{-1}, \tau_q^{-1}, \tau_\nu^{-1}, \tau_\nu^{-1}\right) \tag{4}$$

where τ_ρ and τ_j are conserved quantities associated with density and momentum, respectively, and are typically set to 1; τ_e is related to bulk viscosity, with $\tau_e^{-1} = 1.1$, τ_ζ and τ_q are independently tunable stability-related terms, both taken as $\tau_\zeta^{-1} = \tau_q^{-1} = 1.1$; τ_ν relates to kinematic viscosity ν; $\nu = c_s^2(\tau_\nu - 0.5)\Delta t$. $c_s = 1/\sqrt{3}$ represents lattice sound velocity.

In the moment space, Eq. (1) can be written as (Guo et al., 2002):

$$\mathbf{m}^* = \mathbf{m} - \boldsymbol{\Lambda}(\mathbf{m} - \mathbf{m}^{\mathrm{eq}}) + \Delta t\left(\mathbf{I} - \frac{\boldsymbol{\Lambda}}{2}\right)\mathbf{S} \tag{5}$$

where $\mathbf{m} = \mathbf{M}f$, $\mathbf{I}$ is the unit tensor; $\mathbf{m}^*$ represents the post-collision moment distribution; $\mathbf{S}$ represents the external force term in moment space; $\mathbf{m}^{\mathrm{eq}}$ is the equilibrium moment:

$$\begin{aligned} \mathbf{m}^{\mathrm{eq}} = \mathbf{M}f_\sigma^{\mathrm{eq}} = &\rho_\sigma(1,\ -2+3|\mathbf{u}|^2,\ 1-3|\mathbf{u}|^2, \\ &u_x,\ -u_x,\ u_y,\ -u_y,\ u_x^2-u_y^2,\ u_xu_y)^T \end{aligned} \tag{6}$$

where u_x and u_y represent the velocity components in the x and y directions, respectively, and $|\mathbf{u}|^2 = u_x^2 + u_y^2$. $\rho_\sigma = \sum_\alpha f_{\sigma,\alpha}$ represents the density of component σ.

The Shan-Chen model (Shan and Chen, 1993) is introduced based on the MRT-LBM to realize the addition of external forces such as fluid-fluid interaction force $\mathbf{F}_{\mathrm{int},\sigma}$, fluid-solid interaction force $\mathbf{F}_{\mathrm{ads},\sigma}$, and body force $\mathbf{F}_b$:

$$\mathbf{F}_{\mathrm{int},\sigma}(\mathbf{x},t) = -G_{\sigma\bar{\sigma}}\psi_\sigma(\mathbf{x},t)\sum_\alpha w_\alpha\psi_{\bar{\sigma}}(\mathbf{x}+\mathbf{e}_\alpha\Delta t)\mathbf{e}_\alpha \tag{7}$$

where $\sigma = c$ represents CO$_2$, while $\sigma = o$ denotes the oil phase. The parameter G_{co} characterizes the CO$_2$-oil interaction forces, governing the transition between miscible and immiscible behaviors. ψ is the effective mass, where $\psi = \rho$. The weighting factor w_α is defined as:

$$w_\alpha = \left[\frac{4}{9}, \frac{1}{9}, \frac{1}{9}, \frac{1}{9}, \frac{1}{9}, \frac{1}{36}, \frac{1}{36}, \frac{1}{36}, \frac{1}{36}\right] \tag{8}$$

The fluid-solid interaction force has a similar form to the fluid-fluid interaction force:

$$\mathbf{F}_{\mathrm{ads},\sigma}(\mathbf{x},t) = -G_{\sigma s}\psi_\sigma(\mathbf{x},t)\sum_\alpha w_\alpha s_\sigma(\mathbf{x}+\mathbf{e}_\alpha\Delta t,t)\mathbf{e}_\alpha \tag{9}$$

where $G_{\sigma s}$ is a parameter controlling the strength of fluid-solid interaction force; G_{cs} denotes CO$_2$-solid interaction parameter; and G_{os} denotes oil-solid interaction parameter. The term $s_\sigma(\mathbf{x},t)$ in Eq. (9) can be expressed under the virtual solid density scheme as (Sedahmed et al., 2022):

$$s_\sigma(\mathbf{x},t) = \delta_\sigma(\mathbf{x},t)\tilde{\rho}_\sigma(\mathbf{x},t) \tag{10}$$

where $\delta_\sigma(\mathbf{x},t)$ is a conversion function that takes a value of 1 when a σ-component fluid node contacts a solid node through migration in any of the nine directions, otherwise it is 0. The term $\tilde{\rho}_\sigma(\mathbf{x},t)$ represents the virtual solid density modified by the geometric formula method:

$$\tilde{\rho}_\sigma(\mathbf{x},t) = \chi_\sigma\frac{\sum\limits_\alpha w_\alpha\rho_\sigma(\mathbf{x}+\mathbf{e}_\alpha\Delta t,t)\left[1-\delta_\sigma(\mathbf{x}+\mathbf{e}_\alpha\Delta t,t)\right]}{\sum\limits_\alpha w_\alpha\left[1-\delta_\sigma(\mathbf{x}+\mathbf{e}_\alpha\Delta t,t)\right]} \tag{11}$$

where χ_σ is a parameter controlling fluid wettability. If χ_σ equals 1, it indicates that the fluid is neutrally wet. For a two-phase and two-component system of CO$_2$ and oil, the value of χ_σ is determined by ξ conjugation:

$$\begin{aligned} \chi_c &= 1+\xi \\ \chi_o &= 1-\xi \end{aligned} \tag{12}$$

where $\xi > 0$ indicates that CO$_2$ is the wetting fluid; otherwise, oil is the wetting fluid. The contact angle realized by improving the fluid-solid interaction force format can directly substitute the solid pseudopotential into the calculation of the fluid-fluid interaction force $\mathbf{F}_{\mathrm{int},\sigma}$, which can save some part of the computing resources.

Furthermore, the total external force $\mathbf{F}_\sigma = \mathbf{F}_{\mathrm{int},\sigma} + \mathbf{F}_{\mathrm{ads},\sigma} + \mathbf{F}_{b,\sigma}$ is added to the moment distribution function, and the external force $\mathbf{S}_\sigma$ in the moment space for the σ-component can be written as:

$$\mathbf{S}_\sigma = \begin{bmatrix} 0 \\ 6\left(u_{x,\sigma}^{\mathrm{eq}}F_{\sigma,x} + u_{y,\sigma}^{\mathrm{eq}}F_{\sigma,y}\right) \\ 6\left(u_{x,\sigma}^{\mathrm{eq}}F_{\sigma,x} + u_{y,\sigma}^{\mathrm{eq}}F_{\sigma,y}\right) \\ F_{\sigma,x} \\ -F_{\sigma,x} \\ F_{\sigma,y} \\ -F_{\sigma,y} \\ 2\left(u_{x,\sigma}^{\mathrm{eq}}F_{\sigma,x} - u_{y,\sigma}^{\mathrm{eq}}F_{\sigma,y}\right) \\ \left(u_{x,\sigma}^{\mathrm{eq}}F_{\sigma,y} + u_{y,\sigma}^{\mathrm{eq}}F_{\sigma,x}\right) \end{bmatrix} \tag{13}$$

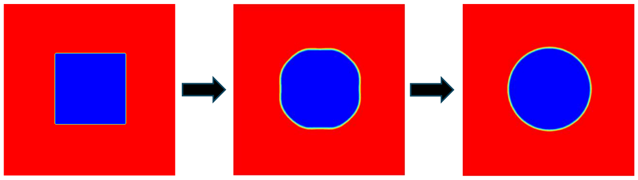

Fig. 1. Morphological evolution of CO_2 under interfacial tension effects. The red area represents oil and the blue area represents CO_2.

where $F_{\sigma,x}$ and $F_{\sigma,y}$ represent the components of the total force $\mathbf{F}_\sigma$ in the x and y directions, respectively. Similarly, $u_{x,\sigma}^{\mathrm{eq}}$ and $u_{y,\sigma}^{\mathrm{eq}}$ represent the components of the equilibrium velocity $\mathbf{u}_\sigma^{\mathrm{eq}}$ in the x and y directions, respectively (Guo et al., 2002), $\mathbf{u}_\sigma^{\mathrm{eq}} = \sum_\sigma \left[\sum_\alpha f_{\sigma,\alpha}\mathbf{e}_\alpha + (\mathbf{F}_\sigma \Delta t)/2\right] / (\sum_\sigma \rho_\sigma)$.

The model also needs to be supplemented with the correct boundary conditions. At the inlet, Zou-He's velocity boundary scheme (Zou and He, 1997) with third-order accuracy is adopted. Given a known velocity value at the boundary, this scheme enables the direct determination of unknown distribution functions at the inlet. To maintain the continuity of physical quantity, a fully developed open boundary condition is applied at the outlet. Specifically, the unknown distribution functions at the outlet are replaced by their counterparts from the adjacent fluid node along the inward normal direction. This approach ensures unimpeded fluid outflow while effectively preventing backflow and unphysical accumulation.

Given the prescribed inlet boundary velocities ($\mu_{x,\sigma}$ in the x direction and $\mu_{y,\sigma}$ in the y direction), the boundary density can be derived from the known distribution functions, which subsequently allows the determination of unknown distribution functions. The density and unknown distribution functions at the inlet can be calculated as:

$$\rho_{\sigma,\mathrm{in}} = \frac{f_{\sigma,0} + f_{\sigma,2} + f_{\sigma,4} + 2(f_{\sigma,3} + f_{\sigma,6} + f_{\sigma,7})}{1 - u_{x,\sigma}} \tag{14}$$

$$f_{\sigma,1} = f_{\sigma,3} + \frac{2}{3}\rho_{\sigma,\mathrm{in}} u_{x,\sigma} \tag{15}$$

$$f_{\sigma,5} = f_{\sigma,7} + \frac{1}{2}(f_{\sigma,4} - f_{\sigma,2}) + \frac{1}{6}\rho_{\sigma,\mathrm{in}} u_{x,\sigma} + \frac{1}{2}\rho_{\sigma,\mathrm{in}} u_{y,\sigma} \tag{16}$$

$$f_{\sigma,8} = f_{\sigma,6} + \frac{1}{2}(f_{\sigma,2} - f_{\sigma,4}) + \frac{1}{6}\rho_{\sigma,\mathrm{in}} u_{x,\sigma} - \frac{1}{2}\rho_{\sigma,\mathrm{in}} u_{y,\sigma} \tag{17}$$

Although the Zou-He velocity boundary scheme achieves high-order accuracy, its stability remains suboptimal, particularly when coupled with MRT collision operators, where special attention must be paid to interaction force calculations at the boundaries. The improved treatment proposed is as follows: When computing interaction forces at the boundary nodes, pseudopotentials migrating outward along all nine discrete directions are replaced by their counterparts from the opposite directions before contributing to force calculations.

3. Model verification

3.1 Laplace test

A square CO_2 is placed at the center of a 100 × 100 lattice simulation domain (lu is lattice units). As the simulation proceeds, the square CO_2 gradually transforms into a circular shape under the influence of interfacial tension (Fig. 1). For multicomponent immiscible systems, the pressure of fluid phase can be given as (Chen et al., 2014):

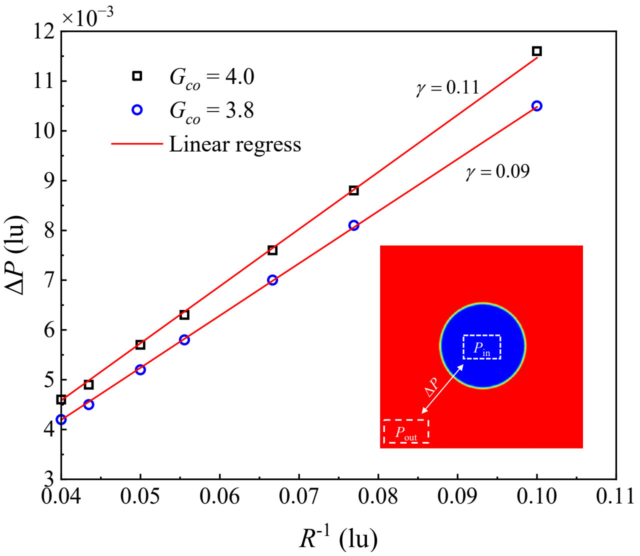

Fig. 2. Laplace tests for different fluid-fluid interaction parameters.

$$p = c_s^2 \sum_\sigma \rho_\sigma + \frac{c_s^2}{2} \sum_{\sigma,\bar{\sigma}} G_{\sigma\bar{\sigma}} \psi_\sigma \psi_{\bar{\sigma}} \tag{18}$$

The pressure difference ΔP between the inside and outside of the droplet is calculated using Eq. (18). According to Laplace's law, ΔP exhibits a linear relationship with the reciprocal of the droplet radius $1/R$, expressed as $\Delta P = \gamma/R$, where the slope corresponds to the interfacial tension γ. Fig. 2 presents the interfacial tension tests under two fluid-fluid interaction force conditions. The corresponding pressure differences are obtained by varying the droplet radii, and on this basis, linear regression is performed. The results show that when G_{co} is 3.8 and 4.0, the corresponding lattice interfacial tensions γ are 0.09 and 0.11, respectively.

3.2 CO_2-oil diffusion

The aforementioned grid size settings are continued to be used for CO_2-oil diffusion validation. When G_{co} decreases to 1.5, there is no longer a distinct phase interface. On this basis, the diffusion degree of CO_2 in the oil phase can be controlled by adjusting the value of G_{co}. When $G_{co} = 0.45$, CO_2 gradually diffuses into the oil phase, and the originally clear phase interface gradually becomes blurred (Fig. 3(a)). This process also satisfies Fick's second law (Chen et al., 2022c):

$$\frac{\partial C}{\partial t} = D\left(\frac{\partial^2 C}{\partial x^2} + \frac{\partial^2 C}{\partial y^2}\right) \tag{19}$$

where C and D represent the density and diffusion coefficient of CO_2, respectively. When t = 260 lu, the CO_2 density distribution curve obtained by Fick's second law is in good agreement with that from LBM simulation (Fig. 3(b)). In addition, through the nonlinear fitting of D and G_{co}, it is found that the two show a cubic polynomial relationship as shown

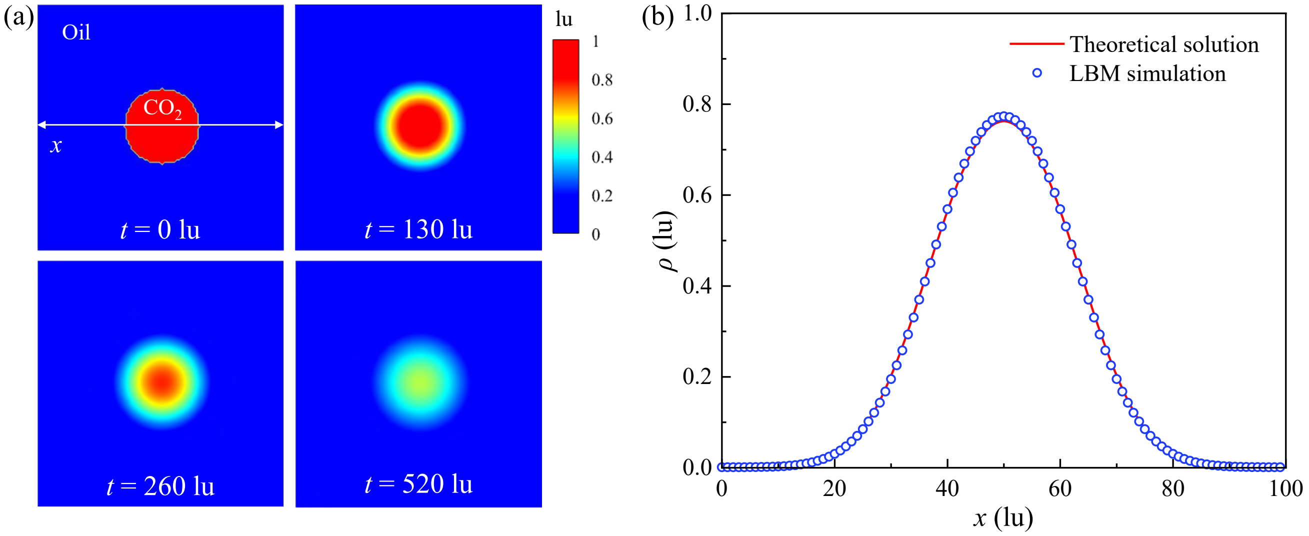

Fig. 3. Verification of CO$_2$ diffusion. (a) Diffusion density distribution of CO$_2$ over time and (b) comparison of CO$_2$ density at the central axis obtained by Fick's second law and LBM at $t = 260$ lu.

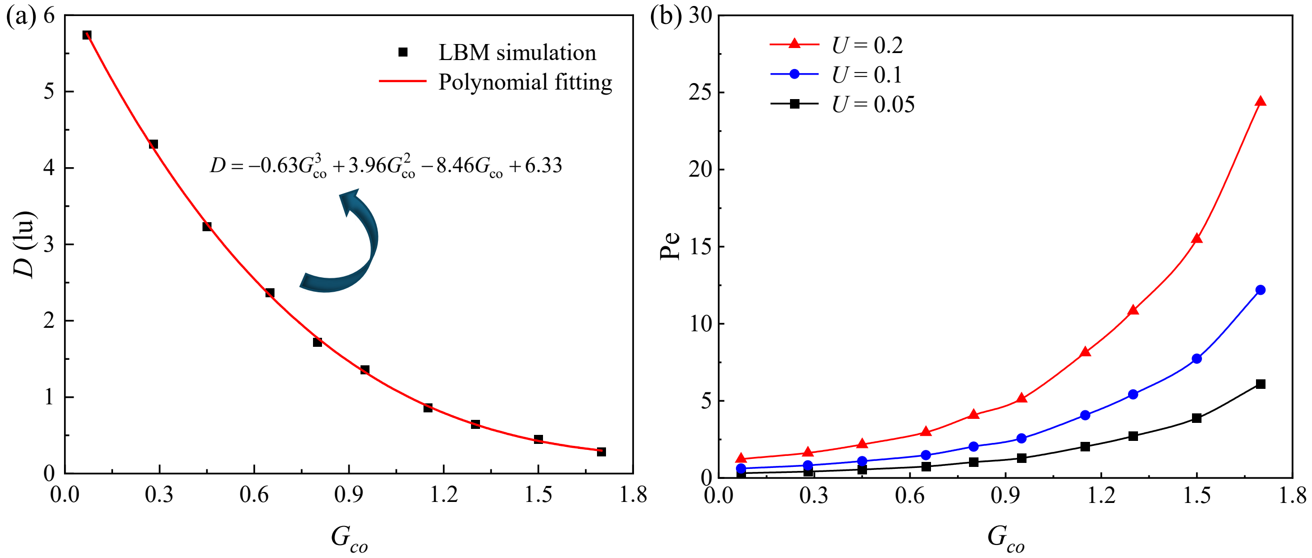

Fig. 4. (a) Relationship between the diffusion coefficient and the fluid-fluid interaction parameter and (b) relationship between the Péclet number and the fluid-fluid interaction parameter.

in Fig. 4(a). Given the fluid-fluid interaction parameter G_{co}, the diffusion coefficient D can be determined directly through their established relationship.

The two most common flow mechanisms in miscible flow simulation are molecular diffusion and viscous flow, and their relative strength can be characterized by the Péclet number (Pe) (Huysmans and Dassargues, 2005):

$$\mathrm{Pe} = \frac{UL}{D} \tag{20}$$

where U represents the lattice velocity of the displacing phase fluid, and L represents the characteristic length, which is selected as 3.5 μm in this work and converted to 35 in lattice units. Under different displacement velocities and CO$_2$-oil interaction parameters, different Pe can be obtained, as shown in Fig. 4(b). Furthermore, based on this correlation chart, the CO$_2$-oil interaction parameter used in the LBM simulation can be derived, provided that Pe and displacement velocity in the actual reservoir are known.

3.3 Contact angle

For immiscible two-phase fluids, the simulation of different contact angles is achieved by introducing fluid-solid interaction forces, and a lattice domain of 200 × 100 is established. The top and bottom of the model adopt the half-way bounce-back boundary, while the left and right sides adopt the periodic boundary. The initial density of the fluid is set as:

$$\rho(x,y) = \begin{cases} \rho_{\mathrm{CO_2}}, & \text{if} \sqrt{(x-x_0)^2 + (y-y_0)^2} \leq R_0 \\ \rho_{\mathrm{oil}}, & \text{otherwise} \end{cases} \tag{21}$$

where the coordinate of the center of the circle is set as $(x_0,\ y_0) = (lx/2,\ 15)$ and the initial radius of the CO$_2$ droplet

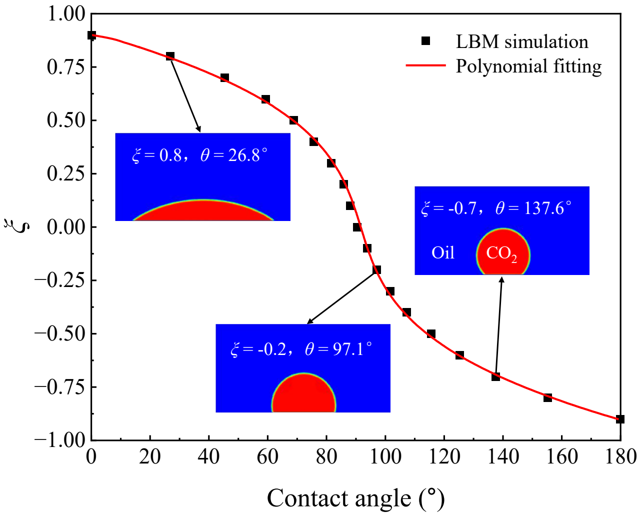

Fig. 5. Polynomial fitting of contact angles under the improved virtual solid density scheme.

is set as $R_0 = 20$. The contact angle can be calculated as:

$$\theta = \begin{cases} \arcsin \frac{a_2}{2r}, & \theta \leq 90^\circ \\ \pi - \arcsin \frac{a_2}{2r}, & \theta > 90^\circ \end{cases} \tag{22}$$

where a_1 represents the height of the droplet and a_2 is the length of the substrate. After the simulation stabilizes, the contact angle can be calculated through conversion using the above formula.

The improved virtual solid density scheme enables more precise control over contact angles. Furthermore, the contact angle exhibits an approximately cubic nonlinear relationship with the fluid-solid interaction adjustment parameter (Fig. 5), expressed as: $\theta = -93.53\xi^3 - 0.97\xi^2 - 22.21\xi + 91.63$. In subsequent studies, as long as the value of ξ is given, the corresponding contact angle θ can be calculated directly.

4. Results and discussion

On the basis of the microstructural characteristics of 2D tight rock cast thin sections observed under scanning electron microscopy, combined with the pore structure distribution obtained through scanning, a region with superior connectivity in the upper right corner was selected to establish the microscopic porous media model shown in Fig. 6. The core sample corresponding to this cast thin section exhibits a gas permeability of 0.25 mD and porosity of 8.8%. The constructed porous media model maintains the same resolution as the 2D cast thin section (0.1 μm), which also serves as the lattice step size for LBM simulations. The model dimensions are 150 × 100 μm^2, corresponding to a lattice domain of 1,500 × 1,000 grid points. The black and white areas in the

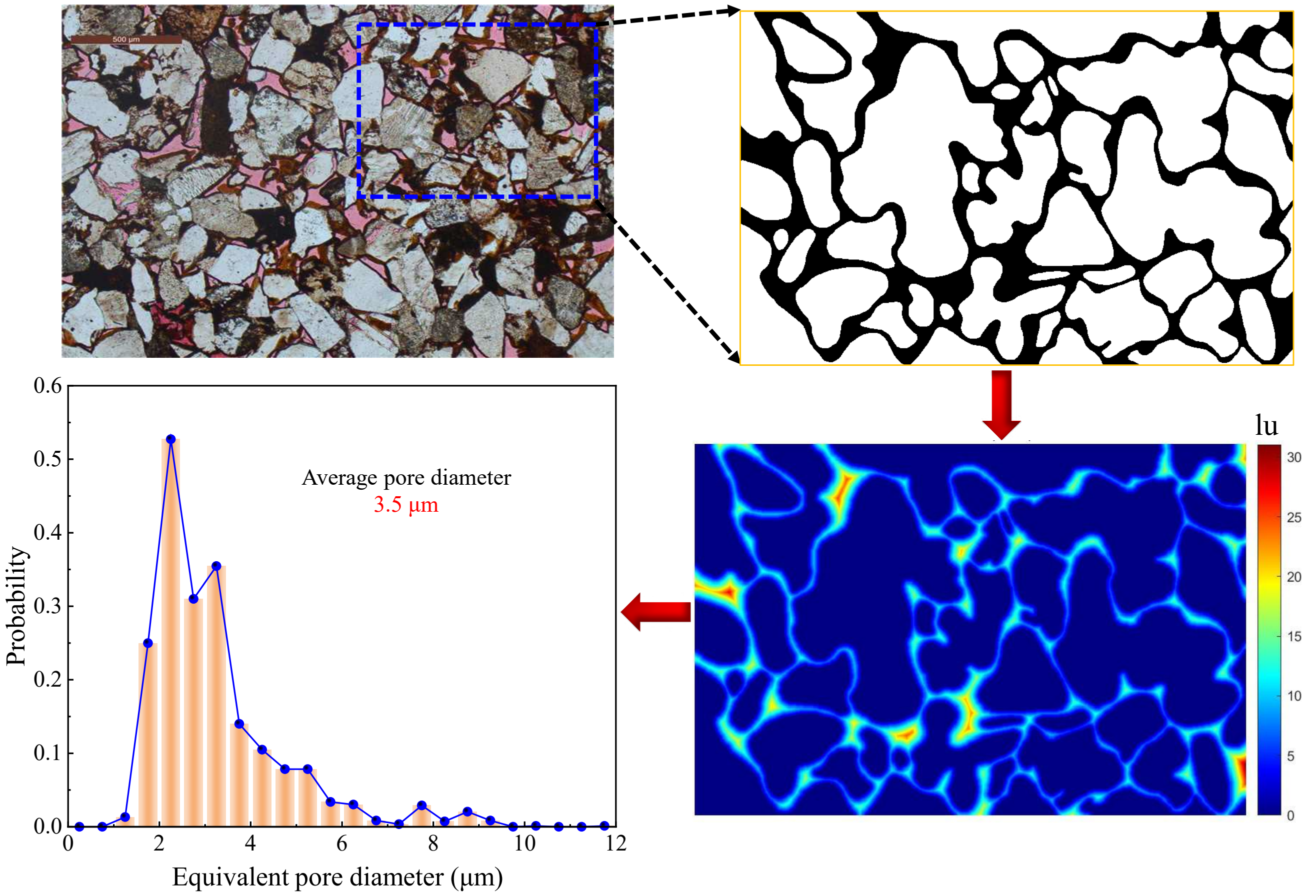

Fig. 6. Porous media model with dimensions of 150 μm (x axis) × 100 μm (y axis) and the corresponding probability distribution of equivalent pore diameters.

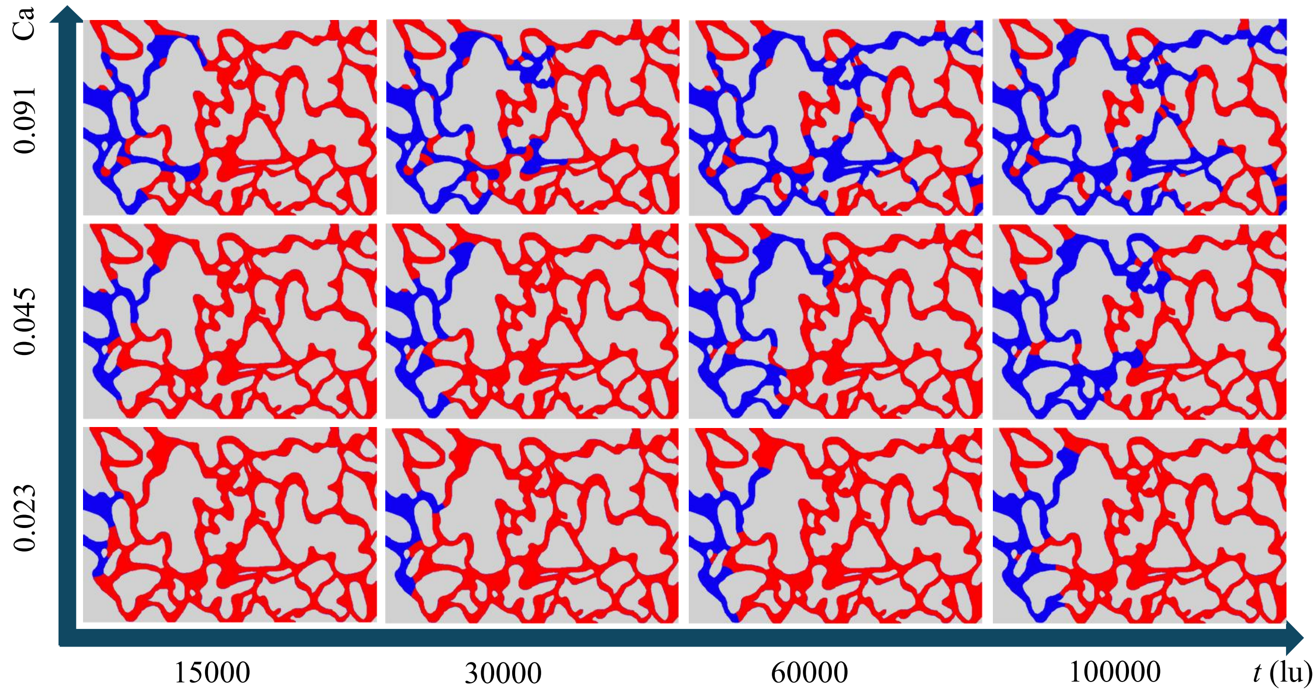

Fig. 7. Evolutionary distribution of CO_2-oil over time under different capillary numbers. The blue area represents CO_2, the red area represents oil, and the gray area is the solid matrix.

model represent pores and matrix, respectively. The upper and lower boundaries as well as the solid walls in the porous media adopt the half-way bounce-back boundary, the inlet adopts the Zou-He velocity boundary, and the outlet adopts the open boundary.

Furthermore, the scanning method was continuously employed to determine the pore size distribution of the model. During this process, the minimum distance from each solid node to the nearest pore node was calculated in all eight adjacent directions. For data smoothing and noise reduction, the resulting minimum distance matrix was processed using Gaussian blurring. The spatial distribution of these minimum distance fields for individual pore nodes is illustrated in the subplot at the lower right corner of Fig. 6. The constructed model exhibits a porosity of 32.7%, representing a nearly fourfold increase compared to the original porosity of the core sample, while it maintains favorable pore connectivity. Furthermore, pore size distribution analysis reveals that the model also possesses a certain degree of heterogeneity. The average pore diameter of this model was calculated to be 3.5 µm, which can serve as the characteristic length L (Zhu et al., 2024). Considering the simplicity of dimensionless units, in the subsequent results and discussions of this work, unless otherwise specified, the simulation parameters are given in lattice units, denoted as lu.

4.1 Effect of capillary number on the immiscible displacement process

The capillary number (Ca) is a dimensionless parameter that evaluates the relative strength of viscous forces to capillary forces (Yiotis et al., 2007), expressed as $\mathrm{Ca} = U\nu/\gamma$. In this section, three different capillary numbers (Ca = 0.023, 0.045, 0.091) are set by varying the displacement velocity U to investigate their effects on CO_2 immiscible displacement. The viscosities of CO_2 and oil are set to 0.05 and 0.25, respectively. The fluid is neutrally wetting ($\xi = 0$), and the interfacial tension $\gamma = 0.11$.

At lower Ca, capillary force dominates. The capillary force in narrow pores increases significantly, causing CO_2 to displace along larger pores as much as possible. Moreover, due to the neutral wetting of the fluid on the pore surface, a small Ca results in a slow advancement rate of the displacement front and low oil recovery. As Ca increases, the viscous force gradually strengthens and the displacement front presents an obvious branched distribution. At this point, the displacement driving force can overcome part of the viscous resistance between pores, effectively expanding the sweep range of CO_2 and forming new seepage channels. When Ca further increases, the viscous force begins to dominate the fluid flow, and the viscous fingering effect caused by the viscosity ratio between CO_2 and oil becomes prominent (Fig. 7). Due to the heterogeneity of the pore structure, CO_2 prematurely breaks through along dominant flow channels, while the displacement process in the non-breakthrough regions gradually slows down.

On the basis of the aforementioned qualitative analysis, a further quantitative assessment was conducted to evaluate the impact of different Ca on oil production. Each point on the curve in Fig. 8 represents oil production at the current time step, and the slope of the curve represents the displacement efficiency. The recovery factor can be calculated based on the oil production corresponding to the right endpoint of the curve and the original reserves. It is evident that at low Ca where

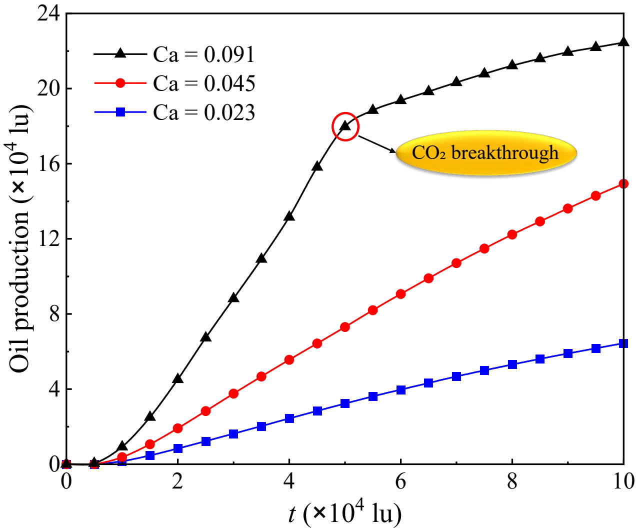

Fig. 8. Variation in oil production with time under different capillary numbers. For Ca = 0.091 and $t = 50,000$ lu, CO_2 breaks through from the oil phase.

capillary forces dominate, both the overall displacement efficiency and ultimate recovery factor remain relatively low. As Ca increases, the enhanced driving force leads to a significant improvement in displacement efficiency and recovery. However, when Ca becomes excessively high, although a higher recovery factor can be achieved, the pronounced viscous fingering effect induced by intensified viscous flow causes CO_2 to break through prematurely along preferential flow channels, ultimately leading to a gradual decline in displacement efficiency.

4.2 Extreme wetting capacity under different displacement velocities

This section focuses on investigating the effects of extreme wettability scenarios under varying displacement velocities on the immiscible displacement processes while elucidating their underlying microscopic mechanisms. The setting of strong CO_2 wettability herein is merely a simulation assumption made to explore the scenario of extreme wettability. Here, two displacement velocities are set, denoted as $U = 0.01$ and 0.02 respectively, to meet the high-velocity and low-velocity conditions require d for extreme wetting. The wettability conditions are represented by $\xi = 0.8$ (strong CO_2-wet) and $\xi = -0.8$ (strong oil-wet), both approaching extreme wettability states.

Under low-velocity and strong CO_2-wet conditions, the pore surfaces exhibit strong CO_2 affinity, causing CO_2 to preferentially displace oil along the pore walls and spread across the surface during slow displacement. Taking the pore surface facing the CO_2 phase as a reference, the capillary force in this case acts as a driving force. Conversely, under low-velocity and strong oil-wet conditions, the pore surfaces exhibit strong oil affinity, forcing CO_2 to advance primarily through the bulk pore space where capillary force acts as a resistance. When the displacement velocity increases to $U = 0.2$, the interfacial morphology at the displacement front undergoes significant changes. The contact angle increases in the strong CO_2-wet case and decreases in the strong oil-wet case, both scenarios leading to weakened capillary effects (Fig. 9). This phenomenon can also be explained by liquid-liquid imbibition mechanisms (Liu et al., 2022): At low velocities, displacement resembles spontaneous imbibition where capillary forces dominate; meanwhile, at high velocities, displacement shifts toward forced imbibition where the driving force suppresses capillary effects, potentially inducing wettability alteration or even reversal.

A further analysis was conducted on the impact of the aforementioned four cases on oil production, with the results illustrated in Fig. 10. Among these, the low-velocity strong oil-wet case exhibit the lowest recovery factor and displacement efficiency due to the capillary force acting as dominant resistance, significantly impeding effective CO_2 displacement. In contrast, for the low-velocity strong CO_2-wet case, where capillary force serves as the driving force (analogous to spontaneous imbibition), both the displacement efficiency and the recovery factor are notably higher than those in the strong oil-wet scenario. Notably, a slight late-stage improvement in displacement efficiency is observed in the low-velocity strong CO_2-wet case, which can be attributed to localized capillary force enhancement caused by the heterogeneous pore structure of the model.

Compared to the low-velocity extreme wettability cases, the high-velocity scenarios achieve higher recovery factors due to the significantly increased driving forces. However, under high-velocity displacement, CO_2 experiences rapid breakthrough through the oil phase, leading to a sharp decline in displacement efficiency post-breakthrough. In the high-velocity strong oil-wet case, CO_2 breakthrough accelerates because although capillary forces are weakened by the driving force, they still act as displacement resistance. This causes CO_2 to bypass smaller pores with higher resistance and preferentially displace oil from larger pores, ultimately breaking through along dominant flow channels. Conversely, in the high-velocity strong CO_2-wet case, while capillary forces are reduced, they remain as displacement drivers. The relatively stronger capillary forces in smaller pores accelerate CO_2 flow into these pore spaces, significantly improving sweep efficiency and resulting in higher recovery compared to the strong oil-wet scenario. Interestingly, the difference in recovery factors between the two high-velocity extreme wettability cases is notably smaller than that observed in low-velocity conditions. This demonstrates that wettability significantly influences low-velocity immiscible displacement processes, while substantial increases in displacement velocity dramatically diminish the wettability effects.

4.3 Péclet number dominates transport mechanisms in miscible displacement

On the basis of the quantitative characterization of G_{co} and D established in Section 3.2, three Pe cases were designed to investigate distinct transport mechanisms during CO_2 miscible displacement. The specific simulation parameters are presented in Table 1. When CO_2 achieves miscibility with oil, the oil viscosity decreases significantly due to CO_2 mass transfer. Therefore, in our miscible displacement simulations, both CO_2

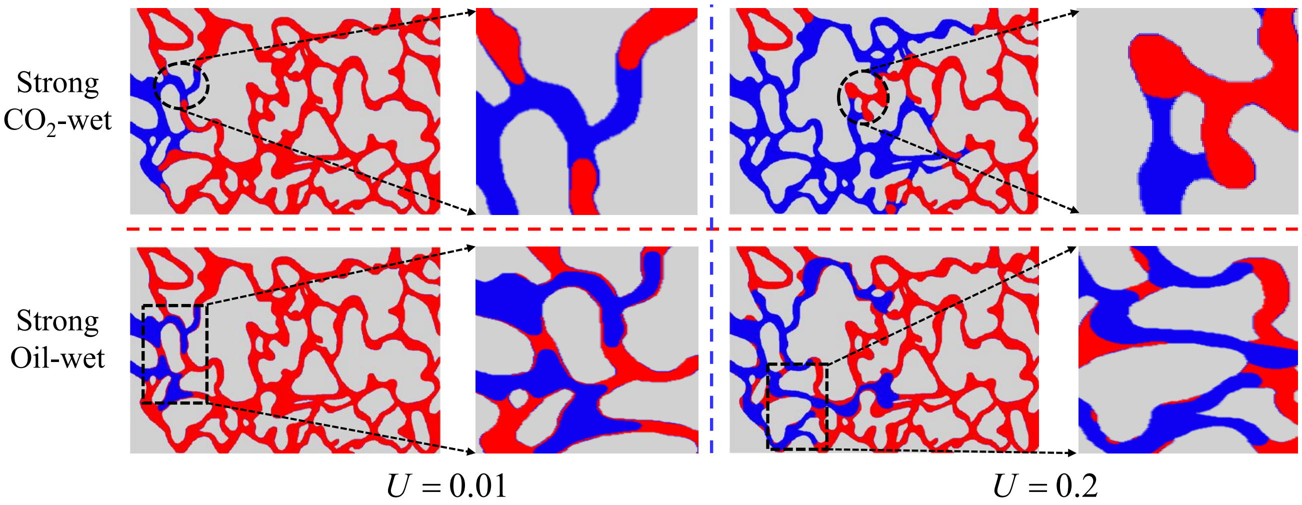

Fig. 9. Evolution of CO_2-oil interface morphology under extreme wettability conditions at varying displacement velocities.

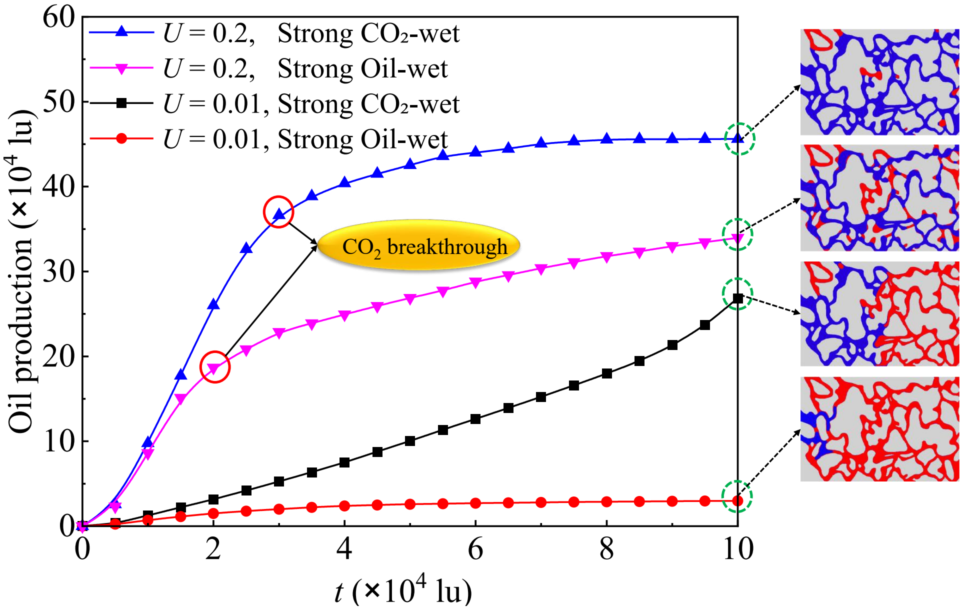

Fig. 10. Temporal variation in oil production under extreme wettability conditions at different displacement velocities. The inset on the right side of the figure illustrates the CO_2-oil distribution at $t = 100,000$ lu for the four scenarios.

Table 1. Parameter configurations for simulations with different Péclet numbers.

Case	G_∞	U	D	Pe
1	0.07	0.05	5.73	0.31
2	0.45	0.1	3.23	1.08
3	1.25	0.2	0.71	9.86

and oil viscosities were set to 0.05. The fluid is neutrally wetting ($\xi = 0$).

At low Pe, molecular diffusion dominates. CO_2 slowly transfers into the oil phase via Fickian diffusion, forming a broad and dispersed miscible front with a gentle concentration gradient. This slow mass transfer significantly reduces the interfacial tension, effectively expands the sweep range of CO_2, while the overall displacement process progresses slowly (Figs. 11 and 12). As Pe increases, viscous flow begins to play a role while molecular diffusion weakens. The miscible front gradually contracts, evolving into a banded structure (Fig. 12). Under the coupling effect of the two mechanisms, both the sweep range of CO_2 and the advancement rate of the displacement process are significantly improved (Fig. 11). When Pe = 9.86, viscous flow becomes significantly stronger, while diffusion effects diminish further. The displacement front further narrows into a tapered (conical) structure (Fig. 12). The enhanced viscous flow further exacerbates displacement instability, as excessively high flow rates may induce CO_2 snap-off at pore throats, leading to the formation of discrete discontinuous phases.

Further analysis was conducted on the temporal variation in oil production under three Pe conditions, with the results

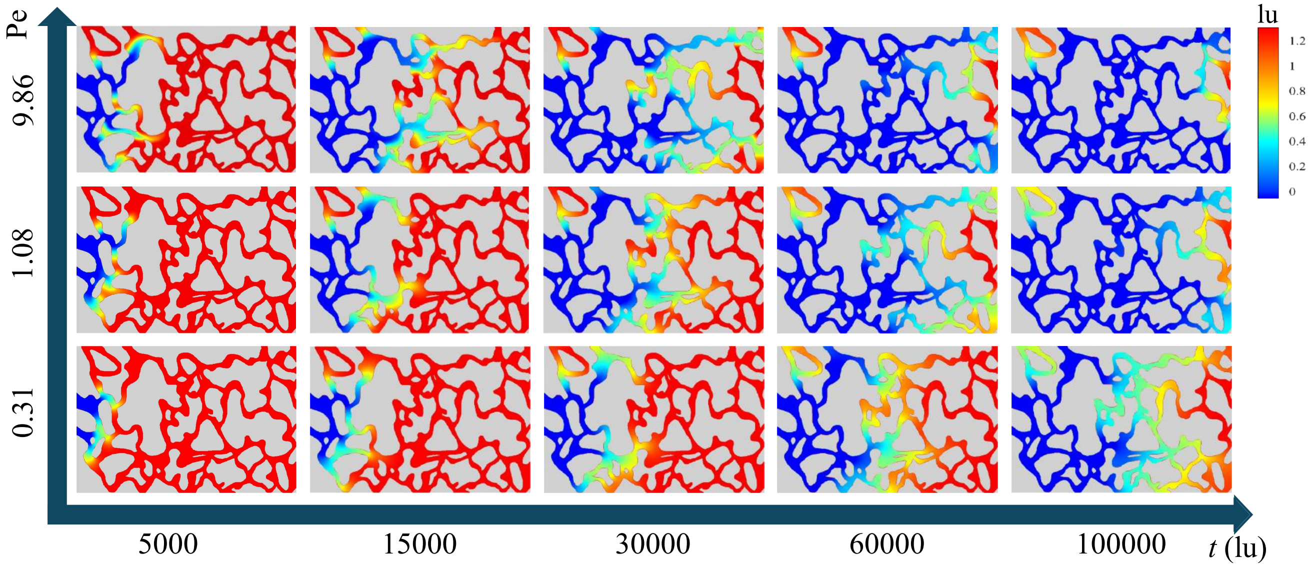

Fig. 11. Temporal evolution of oil density distribution at different Péclet numbers.

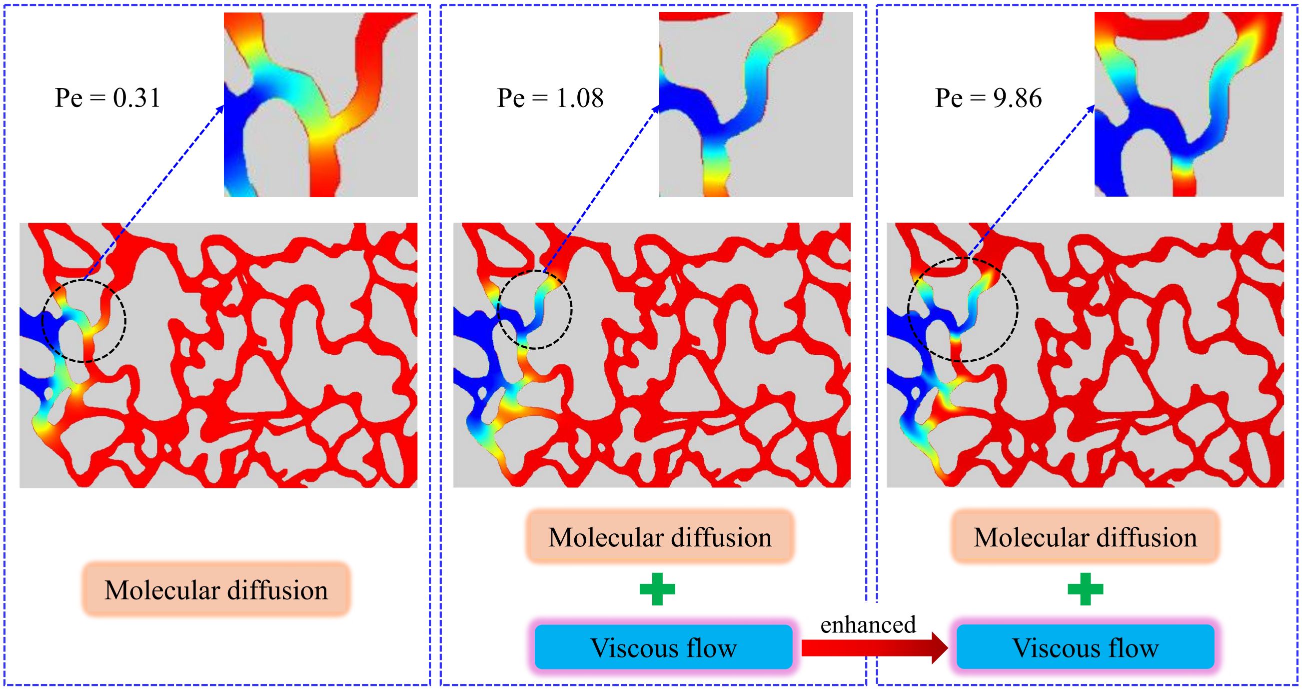

Fig. 12. Schematic diagram of transport mechanisms dominated by different Péclet numbers.

presented in Fig. 13. As Pe increases, the recovery factor shows significant improvement. Notably, after the simulation stabilizes, the case with the smallest Pe exhibits the lowest displacement efficiency, while cases with higher Pe demonstrate a gradual decreasing trend in displacement efficiency. This reduction becomes particularly pronounced when CO_2 rapidly breaks through along dominant flow channels. At Pe = 1.08, a dynamic equilibrium is achieved between molecular diffusion and viscous flow. Although the displacement efficiency decreases following CO_2 breakthrough through preferential channels, it maintains relatively high levels overall. It should be specifically noted that further increasing Pe would lead to viscous flow completely dominating fluid behavior, while molecular diffusion becomes negligible. This would accelerate CO_2 breakthrough in heterogeneous pore structures, severely limiting both the displacement efficiency and the recovery factor. When Pe remains around the unity, the synergistic coupling between these two transport mechanisms can be fully utilized, resulting in satisfactory displacement performance.

4.4 Effect of different injection patterns on the miscible displacement process

Based on the findings detailed in Section 4.3, a fractured porous media model was further constructed, as illustrated in

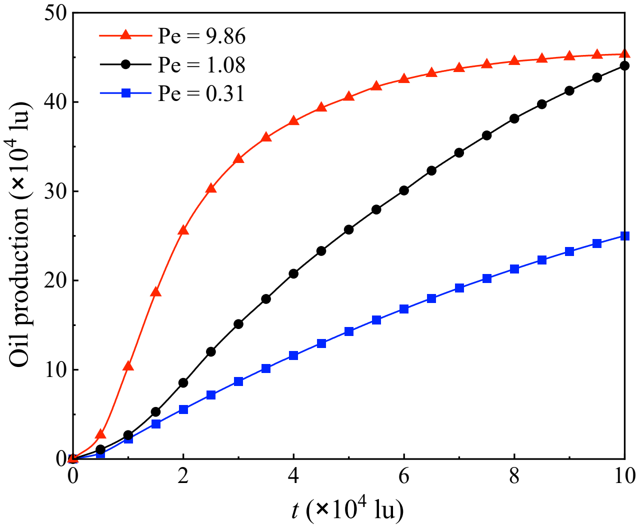

Fig. 13. Variation in oil production with time under different Péclet numbers.

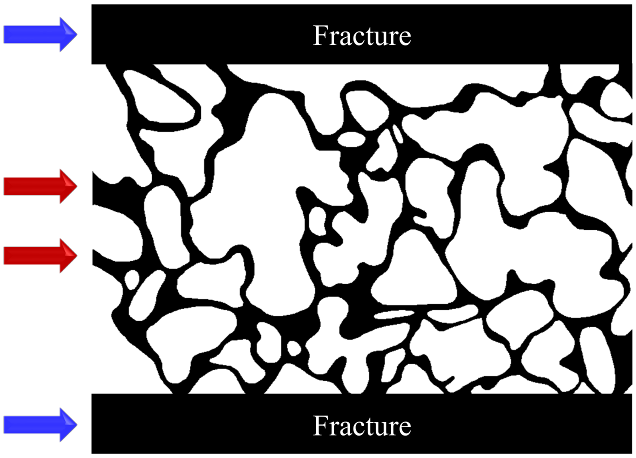

Fig. 14. Porous media model with fractures and different injection patterns (pore injection; fracture injection; fracture-pore injection). The blue arrows indicate the injection of CO_2 through fractures, and the red arrows indicate the injection of CO_2 through pores.

Fig. 14, and the effects of three injection patterns (pore injection; fracture injection; fracture-pore injection) on the miscible displacement process were analyzed. The CO_2-oil interaction parameter was set to $G_{co} = 0.45$, corresponding to a diffusion coefficient $D = 3.23$, and the CO_2 displacement velocity $U = 0.1$. Since the fracture width is significantly larger than the average pore diameter, the resulting Pe is higher than that of the previously discussed porous media model (Alfarge et al., 2017).

For the pore injection mode, CO_2 displaces oil along the middle pores during the initial stage. As the simulation progresses, as some pores are connected to high-permeability fractures, CO_2 gradually shifts to displacing through the fractures. Once CO_2 flows into the fractures, with the continuous injection from the pore end, it primarily displaces the oil within the fractures, while the oil in the middle porous medium remains barely mobilized, resulting in a relatively slow displacement progress (Fig. 15). Under constant-rate injection conditions, when CO_2 flows from narrow pores into the fracture system, its flow pressure gradually decreases, significantly enhancing the molecular diffusion effect during the CO_2 miscible displacement process within the fractures. From the relationship between oil production and time presented in Fig. 16, it can be concluded that this injection mode where pores connect to fractures can achieve relatively stable displacement efficiency and high oil recovery.

In the fracture injection mode, the injected CO_2 first displaces along the fractures. After CO_2 breaks through from the fractures, it gradually shifts from the upper and lower fracture regions to the middle porous medium for displacement (Fig. 15). Unlike the pore injection mode, the CO_2 displacement process under fracture injection has a relatively larger Pe and the effect of viscous flow is more significant. Moreover, due to the high conductivity of fractures, CO_2 will first completely displace the oil in the fractures and then proceed to displace along the interior of the pores. Similarly, the displacement efficiency under the fracture injection mode will drop sharply after CO_2 breaks through along the fractures, and the final oil recovery will also be affected, being the lowest among the three injection modes (Fig. 16).

In the pore-fracture combined injection mode, the CO_2 injected through the dual pore-fracture medium system can efficiently mobilize oil in both the porous medium and the fracture system simultaneously (Fig. 15). It fully leverages the respective advantages of the pore injection and fracture injection modes, achieving the best displacement effect. Moreover, from Fig. 16, it can be clearly concluded that the evolution trend of the oil production curve under this injection mode is similar to that of fracture injection. However, the pore-fracture combined injection can effectively slow down the breakthrough process of CO_2 in the fracture system, enhance the displacement capacity of CO_2 in the porous medium, and achieve the highest oil recovery.

5. Conclusions

The multicomponent multiphase MRT-LBM model constructed in this paper on the basis of pseudopotential scheme can comprehensively account for various CO_2 displacement behaviors. During the immiscible and miscible verification processes, the simulation results obtained by this model are in good agreement with the theoretical test results.

1) The capillary number can quantitatively evaluate the relative strength of viscous forces to capillary forces during immiscible displacement. When the capillary number is small, capillary forces dominate, resulting in lower displacement efficiency/recovery factor. As the capillary number increases, viscous forces gradually become dominant, significantly enhancing the displacement efficiency and recovery. However, excessively high capillary numbers can trigger severe viscous fingering, accelerating CO_2 breakthrough through preferential flow paths and thereby reducing the displacement efficiency.
2) The extreme wetting scenarios under different displacement velocities also significantly influence the CO_2 im-

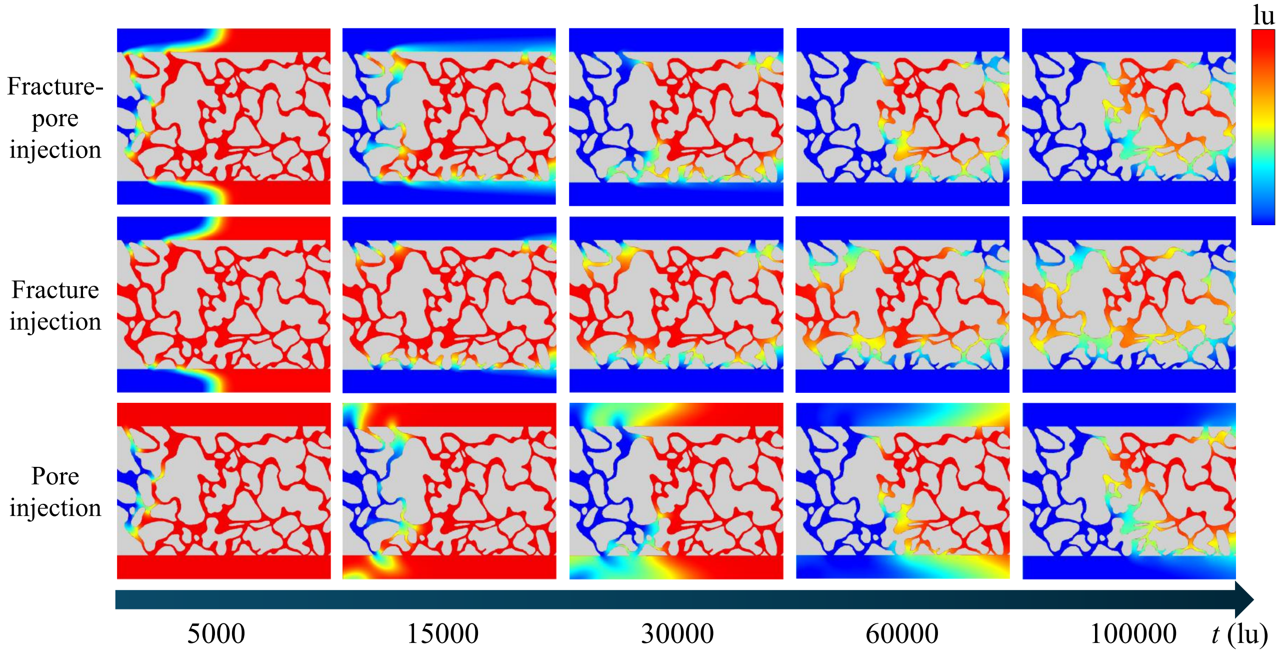

Fig. 15. Temporal evolution of CO_2 density distribution under three injection patterns.

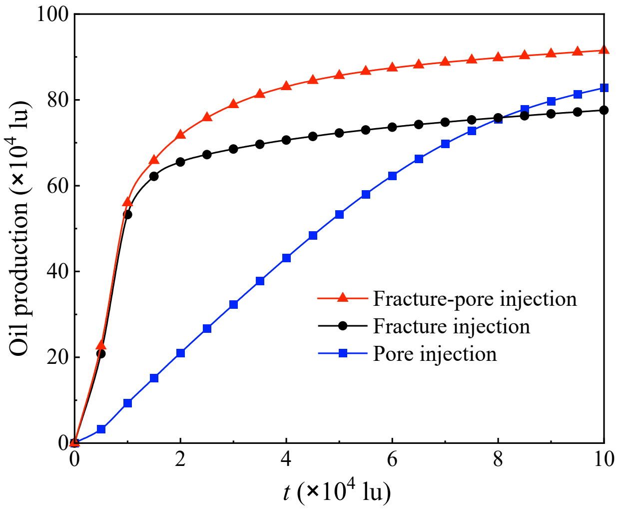

Fig. 16. Variation in oil production with time under different injection patterns.

miscible displacement process. High-velocity extreme wetting yields a superior displacement effect compared to low-velocity conditions. Moreover, an increase in displacement velocity weakens the wetting effect dominated by capillary force, leading to a reduction in the magnitude of difference in oil recovery under high-velocity extreme wetting conditions.

3) In CO_2 miscible displacement, the dominant transport mechanisms governed by the Péclet number lead to distinct displacement outcomes. At low Péclet numbers, molecular diffusion dominates. With a further increase in the Péclet number, viscous flow continues to strengthen while diffusion effects weaken. When the Péclet number is around the unity, the synergistic effect of molecular diffusion and viscous flow is the best.

4) For fractured porous media, different injection patterns also exert a significant impact on the displacement effect. The pore-fracture combined injection mode can not only give full play to the respective advantages of pore injection and fracture injection but also effectively slow down the breakthrough process of CO_2 in the fracture system, achieving the best displacement effect.

Acknowledgements

The authors acknowledge that this study was partially supported by the National Natural Science Foundation of China (Nos. 52174038, U22B2075 and 42172159).

Conflict of interest

The authors declare no competing interest.

References

Alfarge, D., Wei, M., Bai, B. Factors affecting CO_2-EOR in shale-oil reservoirs: Numerical simulation study and pilot tests. Energy & Fuels, 2017, 31(8): 8462-8480.

Bakhshian, S., Hosseini, S. A., Shokri, N. Pore-scale characteristics of multiphase flow in heterogeneous porous media using the lattice Boltzmann method. Scientific Reports, 2019, 9: 3377.

Cai, J., Jiao, X., Wang, H., et al. Multiphase fluid-rock interactions and flow behaviors in shale nanopores: A comprehensive review. Earth-Science Reviews, 2024, 257: 104884.

Chai, Z., Shi, B. Multiple-relaxation-time lattice Boltzmann method for the navier-stokes and nonlinear convection-diffusion equations: Modeling, analysis, and elements. Physical Review E, 2020, 102(2): 023306.

Chen, L., He, A., Zhao, J., et al. Pore-scale modeling of complex transport phenomena in porous media. Progress in Energy and Combustion Science, 2022a, 88: 100968.

Chen, L., Kang, Q., Mu, Y., et al. A critical review of the pseudopotential multiphase lattice boltzmann model: Methods and applications. International Journal of Heat and Mass Transfer, 2014, 76: 210-236.

Chen, H., Liu, X., Zhang, C., et al. Effects of miscible degree and pore scale on seepage characteristics of unconventional reservoirs fluids due to supercritical CO_2 injection. Energy, 2022b, 239: 122287.

Chen, H., Yang, M., Huang, C., et al. A dynamic model of CO_2 diffusion coefficient in shale based on the whole process fitting. Chemical Engineering Journal, 2022c, 428: 131151.

Diao, Z., Li, S., Liu, W., et al. Numerical study of the effect of tortuosity and mixed wettability on spontaneous imbibition in heterogeneous porous media. Capillarity, 2021, 4(3): 50-62.

Ezzatneshan, E., Goharimehr, R. A pseudopotential lattice Boltzmann method for simulation of two-phase flow transport in porous medium at high-density and high–viscosity ratios. Geofluids, 2021, 2021: 5668743.

Frank, F., Liu, C., Alpak, F. O., et al. Direct numerical simulation of flow on pore-scale images using the phase-field method. SPE Journal, 2018, 23(5): 1833-1850.

Gogoi, S., Gogoi, S. B. Review on microfluidic studies for EOR application. Journal of Petroleum Exploration and Production Technology, 2019, 9(3): 2263-2277.

Guo, Z., Zheng, C., Shi, B. Discrete lattice effects on the forcing term in the lattice Boltzmann method. Physical Review E, 2002, 65(4): 046308.

Habibi, A., Yassin, M. R., Dehghanpour, H., et al. Experimental investigation of CO_2-oil interactions in tight rocks: A montney case study. Fuel, 2017, 203: 853-867.

Huysmans, M., Dassargues, A. Review of the use of péclet numbers to determine the relative importance of advection and diffusion in low permeability environments. Hydrogeology Journal, 2005, 13(5): 895-904.

Jia, Z., Cao, R., Wang, B., et al. Effects of CH_4/CO_2 multi-component gas on components and properties of tight oil during CO_2 utilization and storage: Physical experiment and composition numerical simulation. Petroleum Science, 2023, 20(6): 3478-3487.

Lallemand, P., Luo, L. S. Theory of the lattice Boltzmann method: Dispersion, dissipation, isotropy, Galilean invariance, and stability. Physical Review E, 2000, 61(6): 6546.

Li, L., Zhang, D., Su, Y., et al. Microfluidic insights into CO_2 sequestration and enhanced oil recovery in laminated shale reservoirs: Post-fracturing interface dynamics and micro-scale mechanisms. Advances in Geo-Energy Research, 2024, 13(3): 203-217.

Liu, X. Research progress in the evaluation of structural characteristics for tight oil reservoirs. Advances in Resources Research, 2023, 3(1): 1-16.

Liu, Y., Berg, S., Ju, Y., et al. Systematic investigation of corner flow impact in forced imbibition. Water Resources Research, 2022, 58(10): e2022WR032402.

Liu, Y., Min, J., Zhang, X. A novel micro-continuum lattice boltzmann approach for multiscale modeling immiscible two-phase flow in porous media. Physics of Fluids, 2024, 36(8): 083345.

Longde, S., Caineng, Z., Ailin, J., et al. Development characteristics and orientation of tight oil and gas in China. Petroleum Exploration and Development, 2019, 46(6): 1073-1087.

Michels, R., Siebert, D. N., dos Santos, L. O. E. Investigation on the influence of capillary number on drainage in porous media using a lattice Boltzmann method. Journal of Petroleum Science and Engineering, 2021, 205: 108918.

Milad, M., Junin, R., Sidek, A., et al. Huff-n-puff technology for enhanced oil recovery in shale/tight oil reservoirs: Progress, gaps, and perspectives. Energy & Fuels, 2021, 35(21): 17279-17333.

Ozowe, W., Daramola, G. O., Ekemezie, I. O. Recent advances and challenges in gas injection techniques for enhanced oil recovery. Magna Scientia Advanced Research and Reviews, 2023, 9(2): 168-178.

Sedahmed, M., Coelho, R., Warda, H. An improved multi-component pseudopotential lattice Boltzmann method for immiscible fluid displacement in porous media. Physics of Fluids, 2022, 34(2): 023102.

Shan, X., Chen, H. Lattice boltzmann model for simulating flows with multiple phases and components. Physical Review E, 1993, 47(3): 1815-1819.

Shi, K., Chen, J., Pang, X., et al. Wettability of different clay mineral surfaces in shale: Implications from molecular dynamics simulations. Petroleum Science, 2023, 20(2): 689-704.

Wang, H., Cai, J., Su, Y., et al. Pore-scale study on shale oil-CO_2-water miscibility, competitive adsorption, and multiphase flow behaviors. Langmuir, 2023a, 39(34): 12226-12234.

Wang, Y., Cao, R., Jia, Z., et al. A multi-mechanism numerical simulation model for CO_2-EOR and storage in fractured shale oil reservoirs. Petroleum Science, 2024, 21(3): 1814-1828.

Wang, F., Chang, S. Molecular dynamics investigation of shale oil occurrence and adsorption in nanopores: Unveiling wettability and influencing factors. Chemical Engineering Journal, 2024, 481: 148380.

Wang, H., Chen, L., Qu, Z., et al. Modeling of multi-scale transport phenomena in shale gas production – a critical review. Applied Energy, 2020, 262: 114575.

Wang, H., Kang, Q., Wang, W., et al. Oil-CO_2 phase behavior in nanoporous media: A lattice boltzmann study. International Communications in Heat and Mass Transfer, 2025, 163: 108738.

Wang, D., Liu, F., Sun, J., et al. Lattice-Boltzmann simulation of two-phase flow in carbonate porous media retrieved from computed microtomography. Chemical Engineering Science, 2023b, 270: 118514.

Wang, H., Wang, W., Su, Y., et al. Lattice boltzmann model for oil/water two-phase flow in nanoporous media considering heterogeneous viscosity, liquid/solid, and liquid/liquid slip. SPE Journal, 2022, 27(6): 3508-3524.

Yang, J., Boek, E. S. A comparison study of multi-component lattice boltzmann models for flow in porous media applications. Computers & Mathematics with Applications, 2013, 65(6): 882-890.

Yin, Y., Zhang, H. Advances in tight oil reservoir development: A review of CO_2 huff and puff technology. Advances in Resources Research, 2024, 4(3): 280-299.

Yiotis, A. G., Psihogios, J., Kainourgiakis, M. E., et al. A lattice boltzmann study of viscous coupling effects in immiscible two-phase flow in porous media. Colloids and Surfaces A: Physicochemical and Engineering Aspects, 2007, 300(1-2): 35-49.

Zhang, W., Feng, Q., Wang, S., et al. CO_2-regulated octane flow in calcite nanopores from molecular perspectives. Fuel, 2021, 286: 119299.

Zhang, D., Li, L., Wang, H., et al. Study on the mechanism of CO_2 huff-n-puff enhanced oil recovery and storage in shale porous media considering heterogeneous structure. Physics of Fluids, 2024, 36(7): 072005.

Zhang, L., Nowak, W., Oladyshkin, S., et al. Opportunities and challenges in CO_2 geologic utilization and storage. Advances in Geo-Energy Research, 2023, 8(3): 141-145.

Zhang, C., Zhang, Q., Wang, W., et al. Capillary and viscous forces during CO_2 flooding in tight reservoirs. Capillarity, 2022, 5(6): 105-114.

Zhao, J., Qin, F., Kang, Q., et al. A dynamic pore network model for imbibition simulation considering corner film flow. Water Resources Research, 2022, 58(7): e2022WR032332.

Zhou, Y., Guan, W., Zhao, C., et al. Numerical methods to simulate spontaneous imbibition in microscopic pore structures: A review. Capillarity, 2024, 11(1): 1-21.

Zhu, Q., Wu, K., Guo, S., et al. Pore-scale investigation of CO_2-oil miscible flooding in tight reservoir. Applied Energy, 2024, 368: 123439.

Zuo, M., Chen, H., Qi, X., et al. Effects of CO_2 injection volume and formation of *in-situ* new phase on oil phase behavior during CO_2 injection for enhanced oil recovery (EOR) in tight oil reservoirs. Chemical Engineering Journal, 2023, 452: 139454.

Zou, Q., He, X. On pressure and velocity boundary conditions for the lattice Boltzmann BGK model. Physics of Fluids, 1997, 9(6): 1591-1598.